Research Paper

Melting with natural convection with heterogeneous heating sources

Paolo Proia [a],*, Mauro Sbragaglia [b], Giacomo Falcucci [a,c]

[a] *Department of Enterprise Engineering "Mario Lucertini", Tor Vergata University of Rome, Via del Politecnico 1, 00133 Rome, Italy*
[b] *Department of Physics & INFN, Tor Vergata University of Rome, Via della Ricerca Scientifica 1, 00133, Rome, Italy*
[c] *Department of Physics, Harvard University, 17 Oxford Street, 02138 Cambridge, MA, USA*

ARTICLE INFO

ABSTRACT

This study focuses on the dynamics of melting with natural convection in a square enclosure heated from a side boundary (heating source). This is done through an ad-hoc developed numerical model based on the lattice Boltzmann method. The understanding of the convection melting process in such a setup is particularly relevant for the technical exploitation of Phase Change Materials (PCMs) as thermal energy storage and thermal management systems in different applications of technical interest in the field of sustainable energy systems. This study addresses novel and key issues related to the boundary conditions related to the heating source by considering heating sources presenting alternating insulating and conductive patches. The size of the patches has been systematically changed in order to address the role of heterogeneities in the heating source and the heat transfer phenomenon is quantified via the analysis of the dynamics of the average melting front position and the time dependence of the Nusselt number. Side-by-side comparisons between heterogeneous heating sources and homogeneous (conductive) ones are systematically investigated. It is found that the heterogeneity of the boundary conditions changes the dynamics of the heat transfer mechanism introducing additional convective mechanisms of transport that would be absent in the homogeneous case. This study is instrumental to distill engineering principles for the design and development of suitable boundary conditions to exert a passive control on the PCM system for energy storage.

1. Introduction

The phase change from solid to liquid (melting) in the presence of natural convection is ubiquitous in countless phenomena of scientific and technical interest, ranging from geophysical contexts [1–3], to industrial processes [4] and crystal growth [5] just to cite a few examples. In this wide panorama, the heat fluxes generated by thermal convection [6,7] drive local melting of a solid boundary, resulting in a complex dynamical scenario [8–10].

Convection melting is key for the technical exploitation of *Phase Change Materials* (PCMs) as thermal energy storage and thermal management systems, due to their large latent heat [11]. Such a peculiarity allows for the storage and release of large amounts of thermal energy during the phase change process. Several substances, from metals to polymers and beeswax, can be used as PCMs, each presenting its own advantages and disadvantages related to the operating conditions in terms of phase-transition temperature, latent heat and thermal conductivity [12,13]. The adoption of PCMs is known to boost the energetic performance of renewable energy systems, which require energy storage solutions for their proper operation [14]. This is the reason why PCMs have been adopted to realize solar energy storage [15], for

applications ranging from domestic heating [16] to heat pump systems [17]. Recent advances in the understanding of PCMs melting and solidification has led to interesting results in the field of metal hydride management, to boost the capability of hydrogen storage [18–21]. The properties of phase change materials can be designed and adapted to the chosen application during the manufacturing process, for example by mixing multiple materials, adding conductive supports or fillers, or encapsulating the system in a conductive shell. Reviews on these topics are given in [4,13,22–24]. A sketch of convection melting dynamics in a PCM is given in Fig. 1. The PCM is contained in an enclosure and heated from a side boundary under the effect of gravity. After an initial stage dominated by conduction dynamics, the interaction between the temperature gradient and gravity allows for the onset of convection [8]. The hotter liquid rises, promoting melting in the upper region and a non-linear melting front $s = s(y, t)$, defined as the boundary between the liquid and the solid phase, emerges. Given the complexity of the system, both in equations and boundary conditions, there are few analytical results; thus, experiments [8,25] and computer simulations [26–29] are key to assess PCM behaviour [30].

---

* Corresponding author.
 E-mail addresses: paolo.proia@uniroma2.it (P. Proia), sbragaglia@roma2.infn.it (M. Sbragaglia), giacomo.falcucci@uniroma2.it (G. Falcucci).

Nomenclature

Physical quantities

C_p	Specific heat.
$e(t)$	Kinetic energy.
$\vec{F}_g$	Buoyancy force.
$\vec{g}$	Acceleration of gravity.
h	Enthalpy.
L_f	Latent heat of fusion.
L_x, L_y	Dimensions of the system.
p	Fluid pressure.
s	Melting front position.
T	Temperature.
T_0	Reference temperature.
T^∞	Stationary temperature.
T_C	Cold temperature.
T_H	Hot (source) temperature.
T_{nw}	Near-wall temperature.
$\vec{u}$	Fluid velocity.

LBM quantities

$\{\vec{c}\}$	Velocities set.
$\vec{c}_s$	Speed of sound.
f_i, g_i	Distribution functions.
S_i, S_{hi}	Source terms.
w_i	Weights.

Greek symbols

α	Thermal expansion coefficient.
κ	Thermal diffusivity.
λ	Length of insulating patches.
ν	Kinematic viscosity.
ϕ	Liquid fraction.
ρ	Fluid density.
ρ_0	Reference density.
τ, τ_h	LBM relaxation times.
θ	Dimensionless time.

Adimensional numbers

Nu	Nusselt Number.
Pr	Prandtl Number.
Ra	Rayleigh Number.
Ste	Stefan Number.

Boundary Conditions (BCs) play a fundamental role in the convection dynamics [6]: examples include different system inclinations with respect to buoyancy forces [31,32] and heterogeneities of the boundary walls with insulating patches or roughness [3,33–35]. In the presence of a moving boundary in a melting substance, further non-linearities are added to the system [2,7,36,37]. Thus, the impact of boundary conditions in the evolution of convection melting in PCMs is of paramount importance. PCM boundaries are usually assumed as ideal, i.e. homogeneous conductive and/or insulating BCs, but in real situations such boundaries are frequently associated to the onset of heterogeneities, connected to the layout of the boundaries (which frequently are associated with the presence of thermal supports), [13, 38,39] and to non-linear phenomena, such as the detachment from the boundary during solidification [40], which are difficult to predict. Moreover, understanding how a change in BC influences the heat

exchange could provide a way to *passively* control the thermal storage. The impact of BCs on convection melting in PCM's has been studied in some papers in the literature: in [41] the authors studied the effect that a linear variation in the heating temperature plays on the melting of a PCM; in [42] the role of asymmetric flow BCs was investigated; in [43] the authors simulated the effects of protruding heating sources attached to a vertical wall of the enclosure containing the PCM; in [44] the performance of a PCM in porous media in the presence of conductive fins was investigated. In this paper, the role of heterogeneities in the heating source is investigated by studying a simple model of a PCM inside an enclosure (Fig. 1) where the heating source is characterized by a sequence of alternating thermal insulating and conducting patches of length λ. This study hinges on numerical simulations based on the lattice Boltzmann method (LBM) [26,45–48]. LBM is grounded in kinetic theory and offers a series of advantages including an easy modelling of BCs, a feature that is instrumental in the scope of this study. The paper is organized as follows: Section 2 introduces the reference continuum equations for the system under study and recalls the basic ingredients of the LBM used to solve the macroscopic equations for convection melting; in Section 3 some basic benchmark tests for the LBM used are provided; Section 4 presents results and discussions for convection melting in PCM by addressing the importance of heterogeneity in the BC of the heating source; conclusions will follow in Section 5.

2. Problem statement

This section contains the reference equations and general statements for the problem under study. The system is a two-dimensional box of size $L_x \times L_y = L \times L$ with an heating source (left side wall) patterned with a regular array of insulating patches alternating with conductive patches at temperature T_H. The other walls are all insulating and the box is filled with a solid at the melting temperature T_C. The acceleration of gravity is parallel to the heating source, pointing in the negative y direction. The system is sketched in panels (a) and (b) of Fig. 1.

2.1. Macroscopic equations

The equations that describe the fluid dynamics in the system are the continuity equation and the Navier–Stokes equations with a buoyancy force $\vec{F}_g$

$$\partial_t \rho + \vec{\nabla} \cdot \left(\rho \vec{u} \right) = 0 \tag{1}$$

$$\rho(\partial_t + \vec{u} \cdot \vec{\nabla})\vec{u} = \rho \nu \nabla^2 \vec{u} - \vec{\nabla} p + \vec{F}_g \tag{2}$$

where $\vec{u} = \vec{u}(\vec{x}, t)$ is the velocity vector, $\rho = \rho(\vec{x}, t)$ the fluid density, $p = p(\vec{x}, t)$ the fluid pressure and ν the kinematic viscosity (a constant in the case at hand). The Buoyancy term $\vec{F}_g$ is considered in the Boussinesq approximation [6,36]:

$$\vec{F}_g = -\alpha \rho_0 (T - T_0)\vec{g} \tag{3}$$

where T_0 is a reference value for the temperature $T = T(\vec{x}, t)$, ρ_0 a reference value for the density and α the thermal expansion coefficient. Density and momentum dynamics given in Eqs. (1) and (2) are coupled with the advection–diffusion equation with a melting term for the temperature field:

$$\partial_t T + \vec{\nabla} \cdot (T \vec{u}) = \kappa \nabla^2 T - \frac{L_f}{C_p} \partial_t \phi \tag{4}$$

where κ is the thermal diffusivity, L_f the latent heat of fusion and C_p the specific heat of the substance. The field $\phi = \phi(\vec{x}, t)$ is the *liquid fraction*, defined as the relative volume occupied by the liquid phase in a certain position. ϕ depends on the local enthalpy h which in turn depends on the local temperature field T [49]. Before the inception of the phase transition process, no liquid is present in the computational domain, thus $\phi = 0$; when the phase transition is accomplished, only the liquid phase is present, with $\phi = 1$ [13,36].
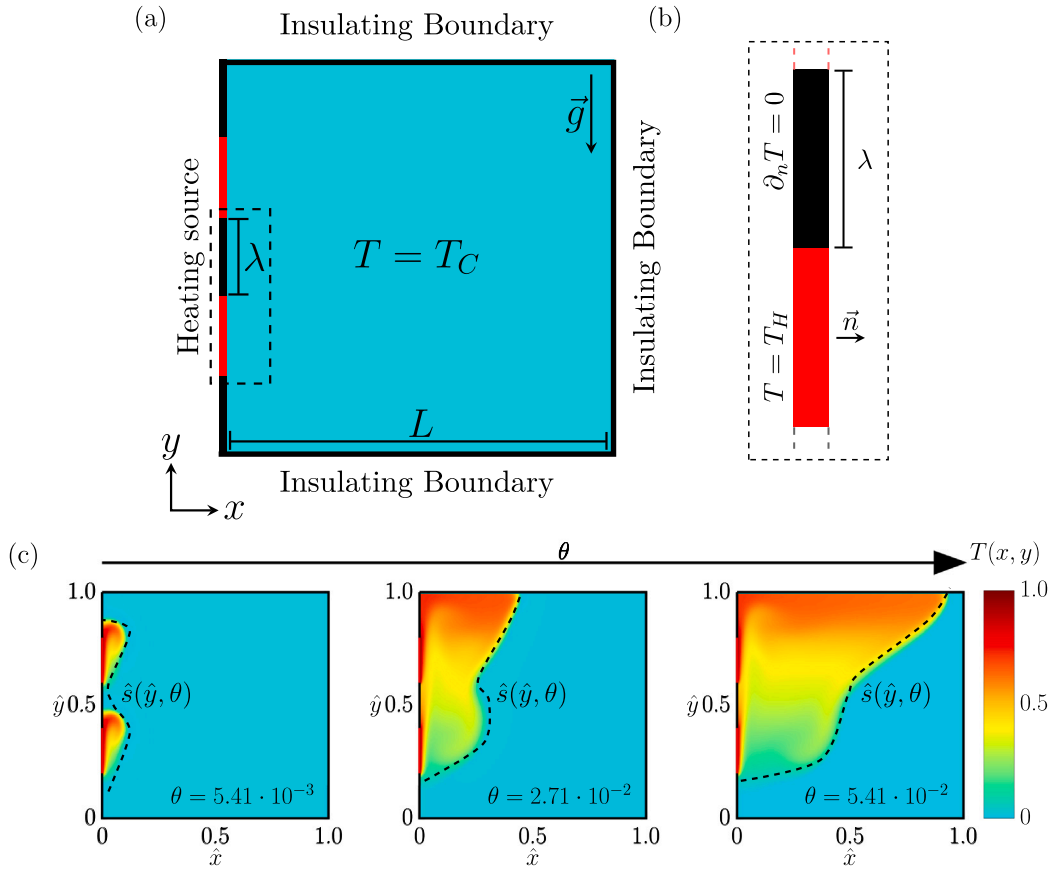
Fig. 1. Panel (a): Sketch of the PCM system with heterogeneous heating source on the left wall, with conductive patches at temperature T_H alternating with insulating patches. The length of the patches is λ (see Panel (b)). All other walls are insulating. The enclosure is filled with a solid at the melting temperature T_C. Panel (c): selected snapshots of the temperature map during the melting process with $\lambda = 0.2 \cdot L$. The dashed line indicates the normalized melting front $\hat{s} = s/L$, where $s = s(\hat{y}, \theta)$ is the melting front location and θ the dimensionless time (see text for details). Spatial coordinates have been made dimensionless with the system size, $\hat{x} = x/L$, $\hat{y} = y/L$.

All the bulk equations above must be coupled with appropriate BCs. For the fluid dynamics part, all boundaries are implemented as no-slip impenetrable walls, implying a zero velocity in contact with the wall

$$\vec{u}_{\text{wall}} = 0. \tag{5}$$

For the thermal dynamics, a heating source and three adiabatic walls are implemented. The heating source is heterogeneous (see Fig. 1), alternating insulating patches with conductive patches. The size of the patches is λ. The BC on the conductive patches is implemented as a constant temperature in time

$$T_{\text{wall}}(t) = T_H = \text{const}, \tag{6}$$

while on the insulating patches (and the insulating walls) zero perpendicular heat flux is imposed as

$$\frac{\partial T}{\partial n}\bigg|_{\text{wall}} = 0 \tag{7}$$

where n is the normal direction to the wall.

To study the dynamics of PCM melting, the following non-dimensional quantities are of relevance:

1. The Rayleigh Number Ra:

$$\text{Ra} = \frac{g\alpha(T_H - T_C)L_y^3}{\nu\kappa}, \tag{8}$$

which is the ratio between buoyancy forces and dissipation;

2. The Stefan Number Ste:

$$\text{Ste} = \frac{C_p}{L_f}(T_H - T_C), \tag{9}$$

that is the ratio between conductive and latent heat;

3. The Prandtl Number Pr:

$$\text{Pr} = \frac{\nu}{\kappa}, \tag{10}$$

given by the ratio between viscous and thermal dissipation;

4. The Nusselt Number Nu:

$$\text{Nu} = \frac{Q}{\kappa(T_H - T_C)}, \tag{11}$$

giving the heat transfer through the left wall (Q) in dimensionless units. In the case of a two dimensional computational domain, Nu can be computed as [8]

$$\text{Nu} = -\frac{\int_0^{L_y} \partial_x T \, (x = 0, y) \, dy}{T_H - T_C}. \tag{12}$$

5. The average melting front position:

$$s_{av}(t) = \frac{1}{L_y} \int_0^{L_y} s(y, t) \, dy. \tag{13}$$

where $s(y, t)$ is the instantaneous melting front position (see Fig. 1).

6. Dimensionless time [19,46]:

$$\theta = \frac{C_p \kappa (T_H - T_C)}{L_f L_y^2} t. \tag{14}$$

When needed, spatial variables will also be made dimensionless with respect to the characteristic size of the system, $\hat{x} = x/L_x$, $\hat{y} = y/L_y$, $\hat{s} = s/L_x$, $\hat{s}_{av} = s_{av}/L_x$.

2.2. The lattice Boltzmann method

The set of continuum equations is solved via a lattice Boltzmann method (LBM). Over the years, the LBM has allowed for the simulations of complex phenomena at the intersection between engineering, physics and, recently, biology [50–53]. In particular, the LBM approach has already been used to simulate the macroscopic equations for convection melting [46,47]. This paper's implementation closely follows the implementation by Huber et al. [46], hence only the main ingredients are recalled here. The LBM is based on the idea of solving the hydrodynamic equations starting from the evolution of probability distribution functions in a discrete kinetic space, $f_i(\vec{x}, t)$, representing the probability to find in the discrete space–time location $(\vec{x}, t)$ a mesoscale particle with kinetic velocity $\vec{c}_i$. The kinetic velocity space is discretized using a finite set of velocities $\vec{c}_i$, $i = 0, \dots, N - 1$ and corresponding weights w_i [54,55]. There are various choices for these sets: for the two dimensional system in this study the choice was the D2Q9 velocity set [54] with $N = 9$ velocities: $\vec{c}_0 = (0, 0)$, $\vec{c}_1 = (+1, 0)$, $\vec{c}_2 = (0, +1)$, $\vec{c}_3 = (-1, 0)$, $\vec{c}_4 = (0, -1)$, $\vec{c}_5 = (+1, +1)$, $\vec{c}_6 = (-1, +1)$, $\vec{c}_7 = (-1, -1)$, $\vec{c}_8 = (+1, -1)$ and weights $w_0 = 4/9$, $w_{1,2,3,4} = 1/9$, $w_{5,6,7,8} = 1/36$. The evolution dynamics of the LBM over a unitary time lapse ($\Delta t = 1$) and unitary grid spacing ($\Delta x = 1$) is:

$$f_i(\vec{x} + \vec{c}_i, t + 1) - f_i(\vec{x}, t) =$$
$$= -\frac{1}{\tau}\left(f_i - f_i^{(\mathrm{eq})}\right)(\vec{x}, t) + \left(1 - \frac{1}{2\tau}\right)S_i(\vec{x}, t). \tag{15}$$

The left side represents the streaming of the PDF, while the right side represents contributions of collision and source terms S_i. Specifically, the simulations at hand make use of the BGK collision operator, which relaxes the particle distribution to its equilibrium $f_i^{(\mathrm{eq})}$ with a characteristic relaxation time τ [54–56]. The discrete equilibrium distribution depends on $(\vec{x}, t)$ via the density and velocity field. The expression for the equilibrium distribution is

$$f_i^{(\mathrm{eq})}(\rho, \vec{u}) = w_i \rho \left(1 + \frac{\vec{c}_i \cdot \vec{u}}{c_s^2} + \frac{(\vec{c}_i \cdot \vec{u})^2}{2c_s^4} - \frac{\vec{u} \cdot \vec{u}}{2c_s^2}\right) \tag{16}$$

where $c_s^2 = \frac{1}{3}$ is the squared speed of sound in the system. The source term S_i depends on $(\vec{x}, t)$ via the velocity field and the external buoyancy force $\vec{F}_g$ (see Eq. (3)). In this study it was modelled according to Guo et al.'s [57] prescription:

$$S_i(\vec{u}, \vec{F}_g) = w_i \left(\frac{\vec{c}_i}{c_s^2} + \frac{(\vec{c}_i \otimes \vec{c}_i) \cdot \vec{u}}{c_s^4} - \frac{\vec{u}}{c_s^2}\right) \cdot \vec{F}_g. \tag{17}$$

From the moments of the distribution in the velocity space one can recover the macroscopic quantities of density and momentum density:

$$\rho = \sum_i f_i = \sum_i f_i^{(\mathrm{eq})}$$
$$\rho \vec{u} = \sum_i f_i \vec{c}_i + \frac{1}{2}\vec{F}_g. \tag{18}$$

It can be shown that the macroscopic quantities ρ and $\rho \vec{u}$ satisfy hydrodynamic equations via an asymptotic expansion known as Chapman–Enskog expansion, whose details can be found in [54,55]. The Chapman–Enskog expansion allows to relate the kinematic viscosity of the fluid to the relaxation time of the LBM [54]

$$\nu = c_s^2 \left(\tau - \frac{1}{2}\right). \tag{19}$$

The LBM can also be used to simulate advection diffusion equations [54,55]. In this paper Eq. (4) was simulated with a second Lattice Boltzmann distribution [46,54,55], $g_i(\vec{x}, t)$, which evolves according to:

$$g_i(\vec{x} + \vec{c}_i, t + 1) - g_i(\vec{x}, t) =$$
$$= -\frac{1}{\tau_h}(g_i - g_i^{(\mathrm{eq})})(\vec{x}, t) + S_{hi}(\vec{x}, t) \tag{20}$$

with equilibrium distribution given by

$$g_i^{(\mathrm{eq})}(T, \vec{u}) = w_i T \left(1 + \frac{\vec{c}_i \cdot \vec{u}}{c_s^2} + \frac{(\vec{c}_i \cdot \vec{u})^2}{2c_s^4} - \frac{\vec{u} \cdot \vec{u}}{2c_s^2}\right). \tag{21}$$

The temperature field is recovered with the zero-th moment of the distribution:

$$T = \sum_i g_i = \sum_i g_i^{(\mathrm{eq})}. \tag{22}$$

To model the melting, one has to model the liquid fraction ϕ first: this was done via a smoothed step function [36] and then by writing it as a function of the enthalpy [36]:

$$\phi(\vec{x}, t) = \begin{cases} 0 & h < h_s \\ \frac{h(\vec{x}, t) - h_s}{h_l - h_s} & h_s \le h \le h_l \\ 1 & h > h_l. \end{cases} \tag{23}$$

where

$$h(\vec{x}, t) = C_p T(\vec{x}, t) + L_f \phi(\vec{x}, t - 1) \tag{24}$$

is the local enthalpy, $h_s = C_p T_C$ the solid enthalpy and $h_l = h_s + L_f$ the liquid enthalpy. At the initial time of any simulation the liquid fraction is set to zero, $\phi(\vec{x}, 0) = 0$, corresponding to a solid system. Thanks to the heat transfer, the enthalpy will change, resulting in a change in the liquid fraction. A lattice site will be considered as liquid if $\phi \ge 0.5$. The melting term enters the LBM dynamics via the source term [46,47]:

$$S_{hi}(\vec{x}, t) = w_i \frac{L_f}{C_p}\left(\phi(\vec{x}, t) - \phi(\vec{x}, t - 1)\right). \tag{25}$$

Finally, the thermal diffusivity is set by the relaxation time of the thermal distribution [54]

$$\kappa = c_s^2 \left(\tau_h - \frac{1}{2}\right). \tag{26}$$

The implementation based on LBM used here closely follows the one used by Huber et al. [46], with the main differences being that here the thermal dynamics is simulated using a D2Q9 velocity set and a second-order (in terms of u) equilibrium distribution instead of a D2Q5 and first-order. While for the thermal LBM a D2Q5 would be sufficient, opting for D2Q9 improves precision (see Section 3 and Fig. 4). The same arguments apply to the choice of a second order thermal equilibrium.

Regarding the BC implementations in the LBM, the no-slip impenetrable wall condition (see Eq. (5)) is implemented via a bounce-back scheme for the populations f_i [54,55]. Regarding the thermal dynamics, the boundary condition on the conductive patch (see Eq. (6)) is implemented by imposing that the thermal distribution function equals an equilibrium distribution with zero velocity and temperature T_H, i.e. $g_i = w_i T_H$. Finally, insulating boundary conditions (see Eq. (7)) are recovered with bounce-back schemes for g_i following Refs. [54,58,59].

3. Benchmarks

Different simulations in different setups were performed to validate the numerical model based on LBM. To test the correct coupling between the temperature dynamics and the momentum balance equation via the buoyancy forces (see Eq. (2)), the problem of transition between conduction and convection in a Rayleigh–Bénard cell [6,60,61] (see Section 3.1) is considered. To check the implementation of the melting term in Eq. (4), the one dimensional Stefan problem is considered. In this system buoyancy forces are neglected and diffusion dominates, resulting in analytical solutions for melting front evolution and temperature distribution [19,22,46] (see Section 3.2). Finally, to validate the model in presence of both convection and melting, simulations for melting dynamics in an enclosure with a homogeneous heating source are conducted and compared with other results available in literature [46] (see Section 3.3).
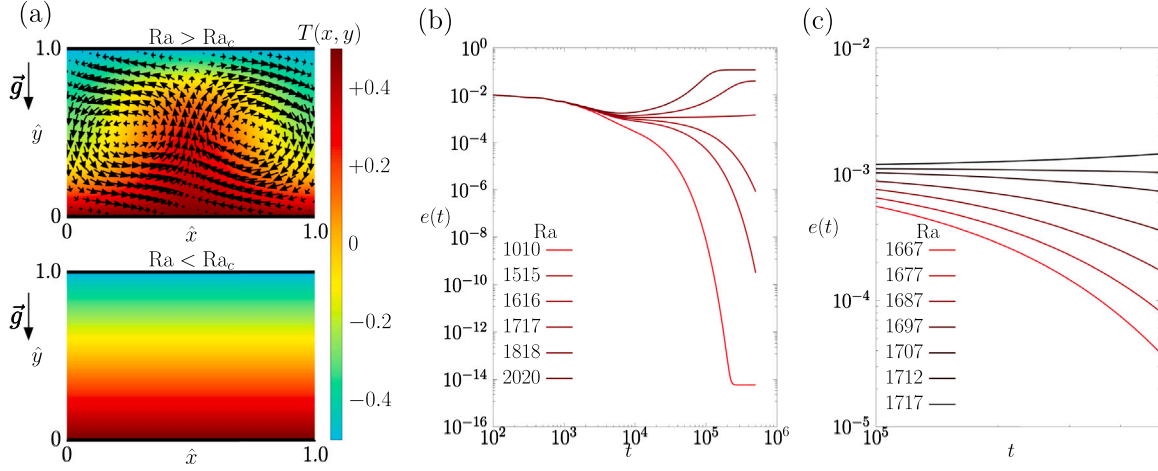
Fig. 2. Transition from conduction to convection in the Rayleigh–Bénard cell. Panel (a) shows the temperature map and the velocity field for the conductive regime ($Ra < Ra_c$) and the convective regime ($Ra > Ra_c$), where Ra is the Rayleigh number (see Eq. (8)) and Ra_c its critical value separating conductive regimes from convective ones. Spatial coordinates have been made dimensionless with the system size, $\hat{x} = x/L_x$, $\hat{y} = y/L_y$. Panels (b) and (c) show plots of the kinetic energy density $e(t)$ (see Eq. (27)) as a function of time for different Ra: $e(t)$ decays for conductive regimes while $e(t)$ reaches a stationary state in convective regimes. The change in behaviour is used to calculate Ra_c.

3.1. Rayleigh-Bénard convection

The Rayleigh–Bénard cell consists of a two-dimensional computational domain of size $L_x \times L_y$, in which the fluid is under the effect of gravity and the melting dynamic is absent ($L_f = 0$ in Eq. (4)). The top and bottom boundaries of the cell are solid no-slip walls, with a hot ($T(x,0) = T_H = 0.5$) and cold ($T(x, L_y) = T_C = -0.5$) temperature source, corresponding to a temperature jump $\Delta T = 1$. Periodic boundary conditions are set at the side boundaries. The interaction between gravity and the thermal gradient triggers a mechanical instability, leading to two possible regimes, depending on the value of Ra. There is, in fact, a critical value Ra_c, dependent on the aspect ratio $\frac{L_y}{L_x}$, that identifies the threshold between conduction and convection inception. If $Ra < Ra_c$ conduction prevails and the system's kinetic energy gets dissipated ($u \to 0$). On the other hand, for $Ra > Ra_c$, the system exhibits a convective dynamics, with the onset of the characteristic vortexes and a heat plume [6]. Panel (a) of Fig. 2 shows a sketch of the two described behaviours. A correct implementation of thermal LBM would deliver an accurate prediction of Ra_c: our benchmark consists in evaluating Ra_c from the simulations to compare with the analytical prediction. Simulation parameters are $L_x = 201$, $L_y = 103$, obtaining $\frac{L_y}{L_x} \approx 0.5$, corresponding to $Ra_c \approx 1707.76$ [6]. The initial temperature is set to a linear profile matching the wall temperatures and the density profile is chosen to satisfy the hydrostatic mechanical equilibrium condition. The velocity field is initialized with an oscillating perturbation, preserving the incompressibility of the flow. Simulations are performed at different Ra by fixing $\tau = \tau_h = 0.8$, (corresponding to Pr = 1), $\rho_0 = 1$, $g = 9.8067$ and varying α. The analysis focused on the behaviour of the kinetic energy $e(t)$, given by:

$$e(t) = \sum_{\vec{x}} \rho(\vec{x}, t) \left| u(\vec{x}, t) \right|^2 . \tag{27}$$

In the conductive regime, $e(t)$ decays, while in the presence of conduction $e(t)$ reaches a stationary value different from zero. The results are shown in panels (b) and (c) of Fig. 2. From the analysis of the simulation data it can be concluded that a critical value for Ra clearly emerges in the range $Ra_c \in (1712.60, 1717,65)$, which is very close (less than 1% error) to the expected value of Ra_c.

3.2. Conduction melting with homogeneous heating source: Stefan problem

The second benchmark test was the simulation of a Stefan problem, i.e. the melting of a solid at the melting temperature T_C with a

heating source at temperature T_H on the left side in the absence of gravity. The absence of gravity makes the melting front uniform and the problem one-dimensional [46,62]. There is an analytical solution (Neumann exact solution) for the temperature field and normalized melting front [8,46]:

$$\begin{cases} T(x,t) = T_H - (T_H - T_C) \dfrac{\text{erf}(x/2\sqrt{\kappa t})}{\text{erf}(\beta)} \\ \hat{s}(t) = \dfrac{s(t)}{L_x} = \dfrac{2\beta}{L_x}\sqrt{\kappa t} \\ \beta \exp(\beta^2) \text{erf}(\beta) = \dfrac{\text{Ste}}{\sqrt{\pi}} \end{cases} \tag{28}$$

where β is an implicit function of the Stefan number and for the chosen parameters ($L_f = C_p = 1 \Rightarrow$ Ste = 1) its value is $\beta \approx 0.62$. This kind of simulation tests the correct implementation of the melting term in the LBM. The considered system is an enclosure with $L_x = 100$, $L_y = 5$, a conductive heating source (see Eq. (6)) at $T_H = 1$ on the left side, an insulating BC (see Eq. (7)) on the right side and periodic boundary conditions on the top and bottom sides. All walls are no-slip (see Eq. (5)). Once a site has melted, it is initialized with $\rho = 1$, $\vec{u} = 0$. Three different simulations were performed using $\tau_h = 2.6, 1.6, 0.6$ corresponding to $\kappa = 0.699, 0.367, 0.033$. The results are shown in Fig. 3. In panel (a) of Fig. 3 the temperature field is plotted as a function of the normalized coordinates for $\kappa = 0.367$, showing that the melting front is uniform. In panel (b) of Fig. 3 simulation results for $\hat{s}$ as a function of θ are compared with the analytical solution given in Eq. (28) for different values of κ. In panel (c) of Fig. 3 simulation results for T as a function of $\hat{x}$ are compared with the analytical solution given in Eq. (28) for different values of κ. Overall an excellent agreement can be observed and it can be concluded that the implementation of the melting term in the temperature equation is correct.

3.3. Convection melting with homogeneous heating source

The final benchmark tests the combined effects of convection and melting by considering the melting of a solid inside a square enclosure of size $L_x = L_y = L$ under the effect of gravity. The left wall of the enclosure is a homogeneous heating source at $T_H = 1$, while the other three walls are insulating (see Eq. (7)). Initially, the solid is at its melting temperature $T_C = 0$. For this system there are no analytical solutions. However, some predictions on the scaling properties of Ra and Nu are available [8,63–65]. For the numerical simulations the
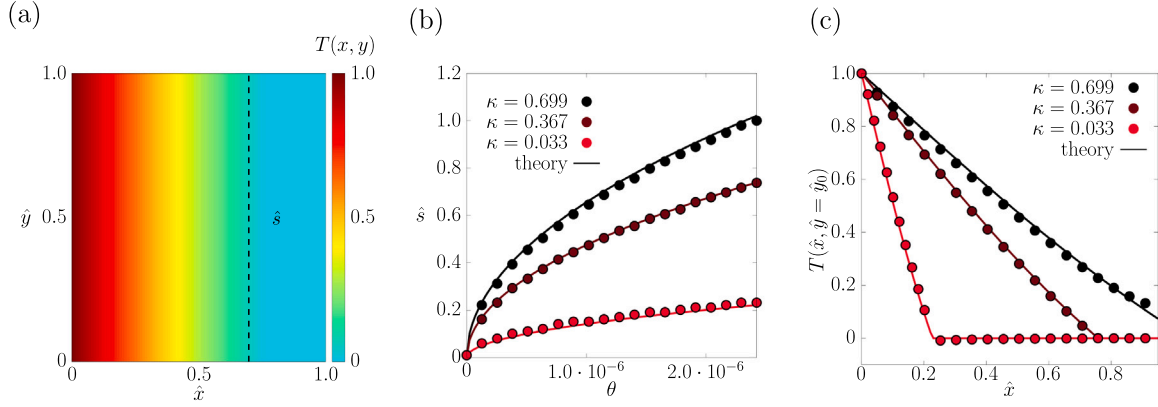
Fig. 3. Melting front dynamics for the Stefan problem. In panel (a) the temperature field is shown at a selected time for thermal diffusivity $\kappa = 0.367$. Spatial coordinates have been made dimensionless with the system size, $\hat{x} = x/L_x$, $\hat{y} = y/L_y$. Panel (b) compares results for the normalized melting front as a function of the dimensionless time θ with the corresponding analytical predictions for different thermal diffusivities κ. Panel (c) shows a comparison between the temperature profile as a function of the normalized coordinate $\hat{x}$ with the corresponding analytical predictions for different thermal diffusivities κ at the selected time $\theta = 2.55 \cdot 10^{-6}$; the vertical coordinate is set to $\hat{y}_0 = 0$. Analytical predictions for melting front and temperature profiles are given in Eq. (28).
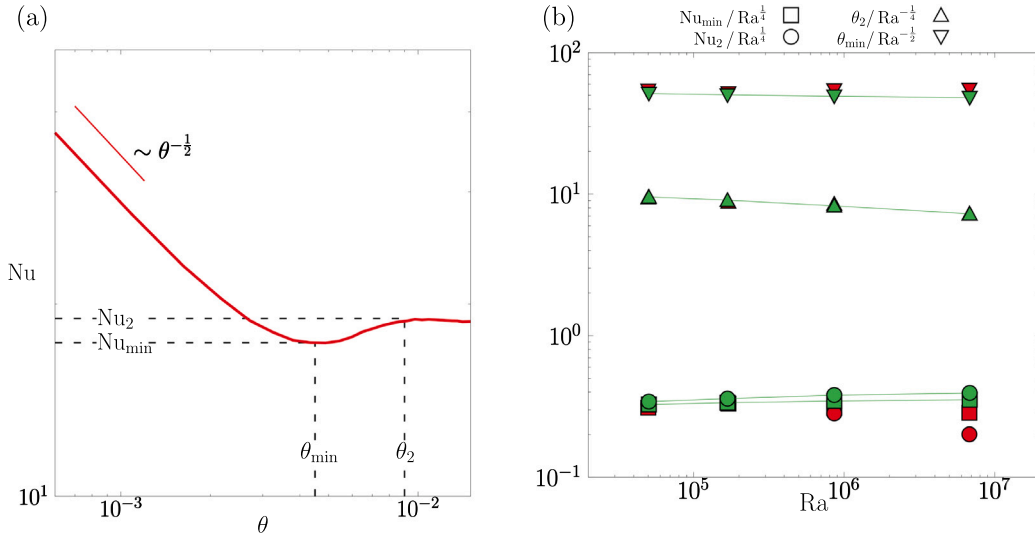

Fig. 4. Panel (a): plot of the Nusselt number Nu as a function of the dimensionless time θ for a case with $\mathrm{Ra} = 10^7$, $\mathrm{Ste} = 10$, $\mathrm{Pr} = 1$. The scaling law $\mathrm{Nu} \sim \theta^{-1/2}$ at small θ is reported; other relevant quantities are indicated (see text for more details). Panel (b): compensated plot for the scaling laws given in Eqs. (30) and (31) as a function of Ra. This paper's data is plotted in green: $\mathrm{Nu}_2 / \mathrm{Ra}^{1/4}$ (●), $\mathrm{Nu}_{\min} / \mathrm{Ra}^{1/4}$ (■), $\theta_2 / \mathrm{Ra}^{-1/4}$ (▲), $\theta_{\min} / \mathrm{Ra}^{-1/2}$ (▼). Corresponding red point s refer to the simulation data by Huber et al. [46].

parameters were set as $L_x = L_y = L = 250$, $\tau = \tau_h = 0.7$, $g = 9.8067$ and $C_p/L_f = 10$, giving $\mathrm{Pr} = 1$ and $\mathrm{Ste} = 10$. Ra was varied as in Section 3.1 and molten sites initialized as in Section 3.2. The parameters are the same as those used in the simulations performed by Huber et al. [46] so that a comparison is possible. The behaviour of Nu as a function of θ is reported in panel (a) of Fig. 4 for a case with $\mathrm{Ra} = 10^7$: Nu first decreases till it reaches a minimum $\mathrm{Nu} = \mathrm{Nu}_{\min}$ at time $\theta_{\min}$; then Nu increases and at time θ_2 the melting front touches the right wall and $\mathrm{Nu} = \mathrm{Nu}_2$; afterwards Nu stays essentially constant. In the limit $\theta \to 0$, the melting process is dominated by conduction and Neumann's exact solution (see Eq. (28)) implies a power-law behaviour in θ with exponent $-1/2$ [8,46]:

$$\mathrm{Nu} \sim \theta^{-\frac{1}{2}} \qquad (\theta \to 0). \tag{29}$$

At later times, due to the inception of convection, other scaling laws are predicted in correspondence of $\theta_{\min}$ [8]:

$$\begin{cases} \theta_{\min} \sim \mathrm{Ra}^{-\frac{1}{2}} \\ \mathrm{Nu}_{\min} \sim \mathrm{Ra}^{\frac{1}{4}} \end{cases}. \tag{30}$$

and in correspondence of θ_2 [8]:

$$\begin{cases} \theta_2 \sim \mathrm{Ra}^{-\frac{1}{4}} \\ \mathrm{Nu}_2 \sim \mathrm{Ra}^{\frac{1}{4}} \end{cases}. \tag{31}$$

From the data reported in panel (a) of Fig. 4 it can be observed that the scaling-law at small times (see Eq. (29)) is in good agreement with the simulation data. The scaling laws given in Eq. (30) and Eq. (31) were further tested using compensated data, i.e. rescaling the quantities $\theta_{\min}$, $\mathrm{Nu}_{\min}$, θ_2, Nu_2 with $\mathrm{Ra}^{-1/2}$, $\mathrm{Ra}^{1/4}$, $\mathrm{Ra}^{-1/4}$, $\mathrm{Ra}^{1/4}$ respectively. These compensated quantities, plotted as a function of Ra for $\mathrm{Ste} = 10$, are shown in panel (b) of Fig. 4. This paper's simulation data (green points) are compared with the simulation results of Huber et al. [46] (red points). It can be seen that compensated data are essentially constant as a function of Ra, indicating a good agreement with the predicted scaling laws [8] (see Eq. (30) and Eq. (31)). Compared to the results of Huber et al. [46] the simulation results show that $\mathrm{Nu}_2 / \mathrm{Ra}^{1/4}$ as a function of Ra displays a more constant trend. This is probably due to a more precise discretization of the advection–diffusion equation via a D2Q9 instead of a D2Q5 and a second-order thermal equilibrium for the thermal dynamics (see Section 2.2 for a more quantitative discussion).
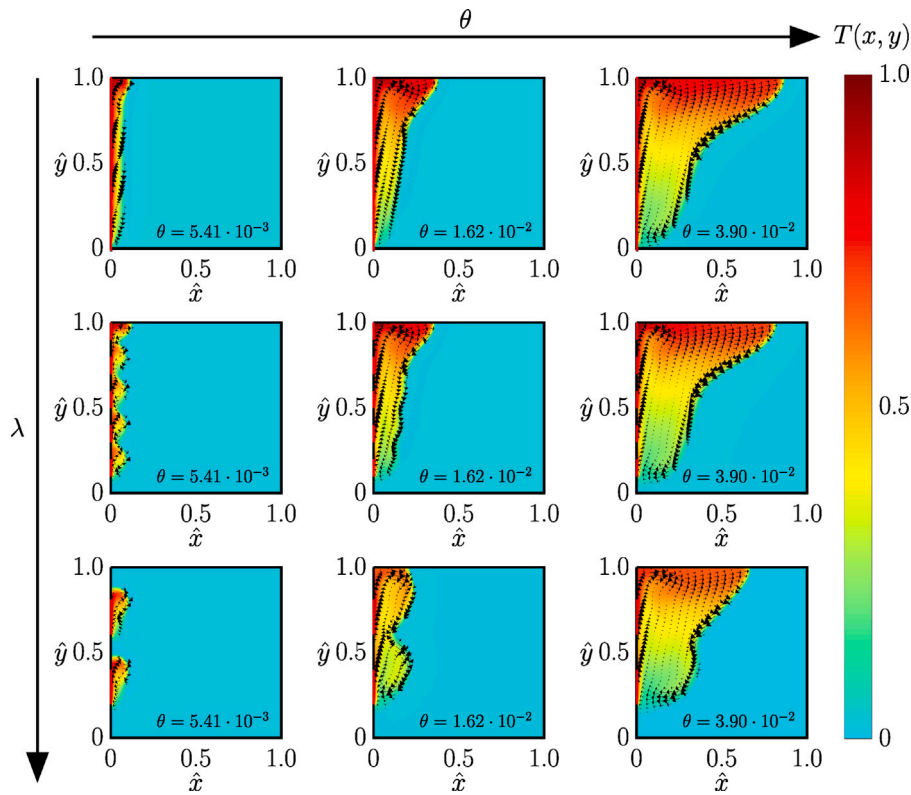
Fig. 5. Plots of the temperature fields with velocity vectors overlaid for different λ and different times, with Ra $= 10^7$ and Ste $= 1$. Spatial coordinates have been made dimensionless with the system size, $\hat{x} = x/L$, $\hat{y} = y/L$. Selected values of $\hat{\lambda} = \lambda/L$ are: $\hat{\lambda} = 0$ (top row), $\hat{\lambda} = 0.1$ (middle row), $\hat{\lambda} = 0.2$ (bottom row).
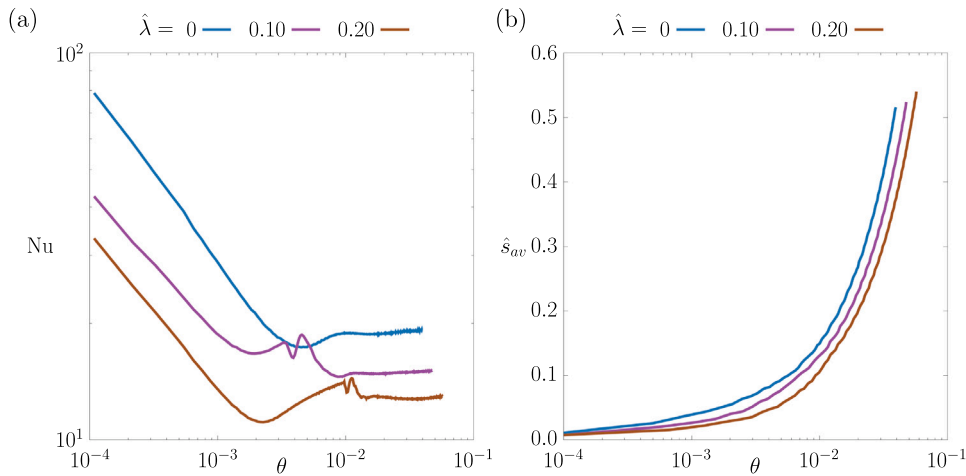

Fig. 6. Panel (a): plot of the Nusselt number Nu as a function of the dimensionless time θ for different values of $\hat{\lambda} = \lambda/L$ with Ra $= 10^7$ and Ste $= 1$. Panel (b): plot of the normalized average melting front position $\hat{s}_{av} = s_{av}/L$ as a function of the dimensionless time θ for different values of $\hat{\lambda} = \lambda/L$.

4. Convection melting with heterogeneous heating source: results and discussions

Results on the effects of the heterogeneities of the heating source are reported in this section. Heterogeneity in the heating source is generated by the insertion of alternating conductive and insulating patches of length λ. A sketch can be seen in panels (a) and (b) of Fig. 1. The value of λ is changed between different simulations. Other simulation parameters are kept fixed to $L_x = L_y = L = 250$, $\tau = \tau_h = 0.7$, $\alpha = 3 \cdot 10^{-4}$, $g = 9.8067$ and $L_f = C_p = 10$, leading to Pr $= 1$, Ste $= 1$, Ra $= 10^7$. In Fig. 5 the evolution in time of the temperature fields with velocity vectors overlaid for different values of $\hat{\lambda} = \lambda/L$ is shown. Time increases along the horizontal direction

while $\hat{\lambda}$ increases along the vertical direction. A significant difference in the dynamics of the system can be seen at increasing $\hat{\lambda}$. In the early stages of the dynamics (left column), an increase in $\hat{\lambda}$ results in the net appearance of distinct thermal plumes which grow in size as $\hat{\lambda}$ grows. Thermal plumes merge at later times, and the merging time appears to increase with increasing $\hat{\lambda}$, implying that the larger is $\hat{\lambda}$ and the longer is the effect of the heterogeneous heating source felt by melting front dynamics. Overall, as $\hat{\lambda}$ increases the melting front gets slower. A more quantitative assessment of this qualitative observation can be done by looking at the Nusselt number Nu and the normalized average melting front $\hat{s}_{av} = s_{av}/L$ as a function of time, which are reported for different values of the dimensionless patch size $\hat{\lambda}$ in panels (a) and (b) of Fig. 6. Regarding the Nusselt number reported in panel (a), the
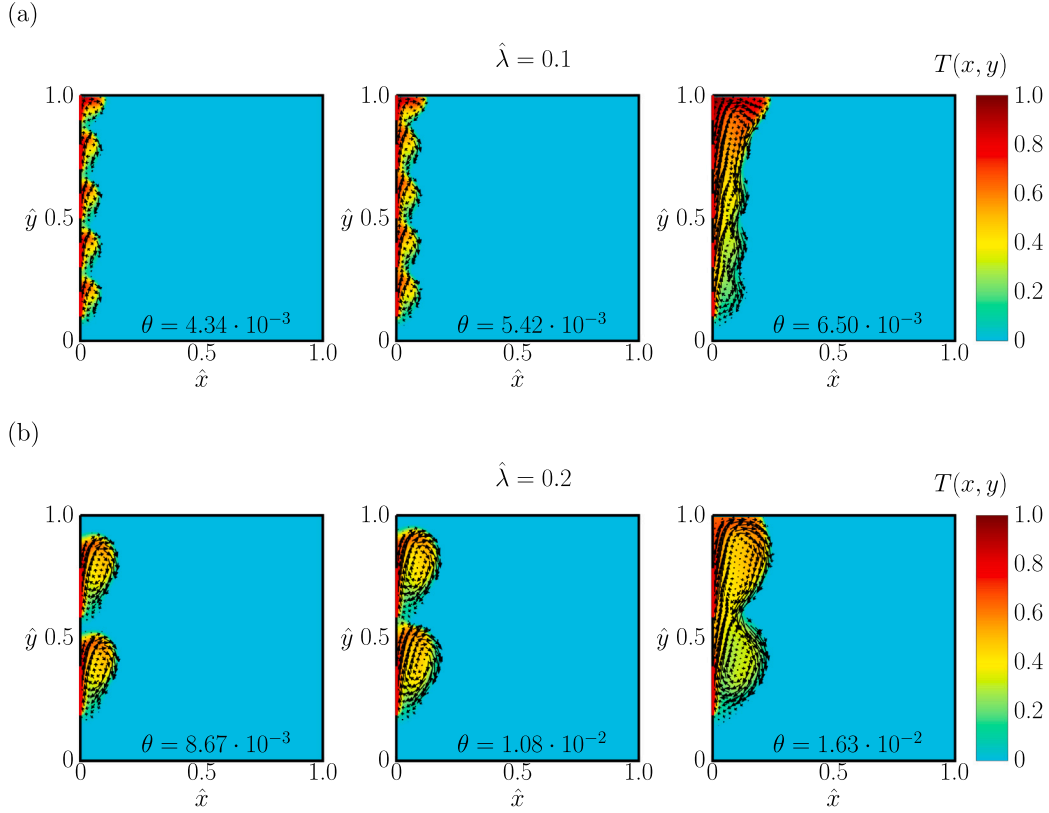
(a)

(b)

Fig. 7. Plots of the temperature fields with velocity vectors overlaid for $\hat{\lambda} = 0.1$ (top row) and $\hat{\lambda} = 0.2$ for different times in the early stage of the dynamics. For both systems $Ra = 10^7$ and $Ste = 1$. Spatial coordinates have been made dimensionless with the system size, $\hat{x} = x/L$, $\hat{y} = y/L$.
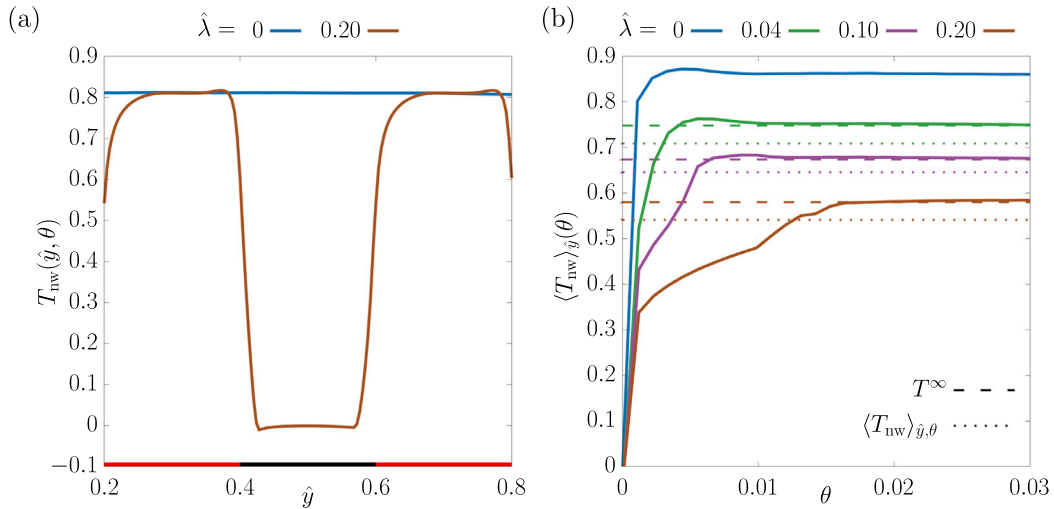
(a)   (b)

Fig. 8. Panel (a): near-wall temperature $T_{nw}(\hat{y}, \theta)$ (see text for details) as a function of the normalized vertical coordinate $\hat{y} = y/L$ for $\hat{\lambda} = 0$ and $\hat{\lambda} = \lambda/L = 0.20$ with $Ra = 10^7$, $Ste = 1, Pr = 1$ and fixed $\theta = 1.08 \cdot 10^{-3}$. Panel (b): average of the near-wall temperature $\langle T_{nw} \rangle_{\hat{y}}(\theta) = \int_0^1 T_{nw}(\hat{y}, \theta) \, d\hat{y}$ as a function of θ for different values of $\hat{\lambda} = \lambda/L$.

phenomenology that is observed for homogeneous boundary conditions ($\hat{\lambda} = 0$) stays qualitatively unchanged in presence of heterogeneous heating sources ($\hat{\lambda} \neq 0$), although Nu starts from smaller values for $\theta \ll 1$, due to the reduced heat flux generated by the heterogeneous heating source. Regarding the plot of $\hat{s}$ reported in panel (b), lower values of $\hat{s}$ can be similarly observed for a fixed time at increasing $\hat{\lambda}$. It is important to notice that when $\hat{\lambda} \neq 0$ oscillations appear in the plot of Nu as a function of θ (panel (a) of Fig. 6) for θ slightly larger than θ_{min}. An explanation for these oscillations can be found in Fig. 7, which shows snapshots of the temperature fields in the early stage of

the dynamics: oscillations in Nu are indeed symptomatic of interactions between the different convective thermal plumes and essentially appear for those times when plumes merge.

In presence of insulating patches the area of the heated surface obviously changes. Thus, one also has to consider the effect of a change in the heated area. To delve deeper into this point, in Fig. 8 the temperature profiles in the near-wall region $T_{nw}(\hat{y}, \theta)$ are analysed by looking at the temperature field at a fixed distance $\ell_{nw} = 8 \cdot 10^{-3} L$ from the heating source, i.e. $T_{nw}(\hat{y}, \theta) = T(\hat{x} = \ell_{nw}/L, \hat{y}, \theta)$. Panel (a) of Fig. 8 shows the profiles of $T_{nw}(\hat{y}, \theta)$ as a function of $\hat{y}$ for a fixed
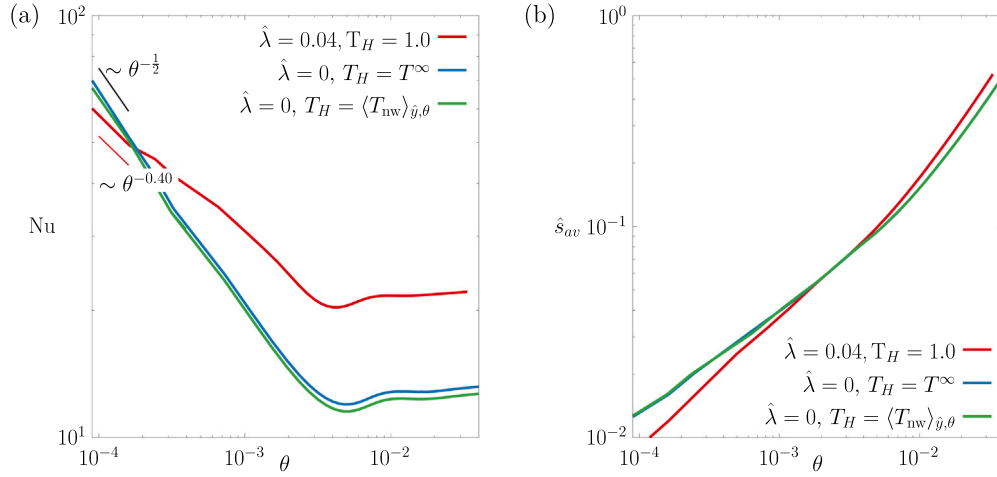
Fig. 9. Plot of the Nusselt number Nu (Panel (a)) and normalized average melting front $\hat{s}_{av}$ (Panel (b)) as a function of the dimensionless time θ for a case with heterogeneous heating source ($\hat{\lambda} = \lambda/L = 0.04$, Ra $= 10^7$, Ste $= 1$, Pr $= 1$) and two cases with homogeneous heating source. In the case with heterogeneous heating source, the near-wall temperature T_{nw} was computed (see Fig. 8 and text for more details) and then the temperature of the homogeneous heating source T_H was set to the stationary value of the near-wall temperature, $T_H = T^\infty$, or to the space–time average of the near wall temperature, $T_H = \langle T_{\text{nw}} \rangle_{\hat{y},\theta}$. In Panel (a) The early stage of the dynamics of the heterogeneous heating source is well fitted with a scaling law Nu $\sim \theta^{-a}$ with exponent that differs from $-1/2$. For the selected case $\hat{\lambda} = 0.04$ an exponent $a \approx 0.40$ was found. Other scaling exponents for different values of $\hat{\lambda}$ are given in Table 1.

$\theta = 1.08 \cdot 10^{-3}$ and different values of $\hat{\lambda}$. While in correspondence of the conductive patches (red segment in the x axis) the temperature approaches the value of the corresponding homogeneous system ($\hat{\lambda} = 0$), in correspondence of the insulating patches (black segment in the x axis) the temperature remains very small. Panel (b) of Fig. 8 shows the spatial average of the near-wall temperature, $\langle T_{\text{nw}} \rangle_{\hat{y}}(\theta) = \int_0^1 T_{\text{nw}}(\hat{y}, \theta) \, d\hat{y}$, as a function of time for different values of $\hat{\lambda}$. Overall, $\langle T_{\text{nw}} \rangle_{\hat{y}}(\theta)$ first shows an increase before going to a steady state with a stationary value T^∞. Two major effects emerge at increasing $\hat{\lambda}$: first, when $\hat{\lambda}$ gets larger, the time it takes for $\langle T_{\text{nw}} \rangle_{\hat{y}}(\theta)$ to reach the stationary state gets larger, roughly increasing proportionally with $\hat{\lambda}$. Second, the stationary value T^∞ decreases as $\hat{\lambda}$ increases: as highlighted in panel (a), this is due to the effect of heterogeneous heating source, resulting in near wall temperature profiles that are heterogeneous along the vertical direction and on average smaller than the corresponding values of T_H. Thus, in order to promote a fair comparison between heterogeneous and homogeneous heating sources, it would be desirable to consider a simulation with a heterogeneous heating source, extract the near-wall temperature $T_{\text{nw}}(\hat{y}, \theta)$, and perform a simulation with a homogeneous heating source with $T_H(\theta) = \langle T_{\text{nw}} \rangle_{\hat{y}}(\theta)$. To make progress in this direction, for a given value of $\hat{\lambda}$, additional simulations were performed with $\hat{\lambda} = 0$ and the heating source temperature T_H set to the stationary value of the near-wall temperature ($T_H = T^\infty$, protocol 1) or to the space–time average of the near wall temperature ($T_H = \langle T_{\text{nw}} \rangle_{\hat{y},\theta}$, protocol 2). The time average is computed in the interval $[0, \theta_2]$. In Fig. 9 Panel (a) the behaviour of Nu is shown as a function of θ by comparing a simulation with $\hat{\lambda} = 0.04$ and two simulations with $\hat{\lambda} = 0$ with T_H chosen based on the two protocols. Note that for these quantitative comparisons between homogeneous and heterogeneous heating sources, we adopt the definition of Nu in Eq. (11) and the definition of θ in Eq. (14) with $T_H = T^\infty$. In Fig. 9 Panel (b) the average normalized melting front $\hat{s}_{av}$ is shown as a function of θ. First of all, it can be observed that simulation results with $\hat{\lambda} = 0$ based on the two protocols deliver very similar outcomes: indeed, the value of T^∞ is only slightly larger than $\langle T_{\text{nw}} \rangle_{\hat{y},\theta}$ due to the fact that the transient dynamics of the near-wall temperature does not take the majority of the time θ_2 needed for the melting front to touch the right wall. It is therefore to be expected that performing a simulation with $\hat{\lambda} = 0$ and dynamical source temperature $T_H(\theta) = \langle T_{\text{nw}} \rangle_{\hat{y}}(\theta)$ would not change too much results with $\hat{\lambda} = 0$ in Fig. 9. In the early stage of the dynamics, data with homogeneous and heterogeneous heating sources behave

Table 1
Characterization of the early and late stage dynamics of Nu as a function of θ for different values of λ. In the early stage of the dynamics, simulation data are fitted with the functional behaviour Nu$(\theta) = b + \theta^{-a}$. The late stage of the dynamics is characterized by θ_2. Values for a, b and θ_2 are reported for different values of λ.

λ	$\hat{\lambda} = \lambda/L$	a	b
5	0.02	0.43	4.57
10	0.04	0.40	6.33
25	0.1	0.37	7.78
50	0.2	0.35	3.38

differently: for the homogeneous heating source it can be observed that Nu $\sim \theta^{-1/2}$; for the heterogeneous heating source, instead, fitting the data for small θ with the functional behaviour Nu$(\theta) = b + \theta^{-a}$ yields different exponents a for different values of λ. Results are summarized in Table 1. The scaling behaviour Nu $\sim \theta^{-1/2}$ is peculiar of a scenario where conduction mechanisms dominate (see Fig. 4 and Eq. (29)), hence a change in the scaling exponent could be related to the presence of convective rolls that are triggered by the heterogeneous heating source and appear in the early stages of the dynamics (see Fig. 7). At the present stage of the analysis, it cannot be claimed that the behaviour of Nu as a function of time is exactly a power-law, rather this could be an interesting theoretical topic to develop for future research. Moreover, in the plot related to the Nu it is observed that the process of melting in presence of heterogeneous heating sources produces larger Nu at later times, a fact that is probably related to the overall enhanced convection that is triggered by the heterogeneous pattern.

Finally, in Fig. 10 we explore the effect of a change in Ra by comparing cases with heterogeneous heating sources with $\hat{\lambda} = 0.04$ and $T_H = 1$ and the case with homogeneous heating source with $\hat{\lambda} = 0$ and $T_H = T^\infty$. We adopt the definition of the Rayleigh number given in Eq. (8) with $T_H = T^\infty$. We look at compensated data for $\theta_{\min}$, Nu$_{\min}$, θ_2, Nu$_2$, similarly to the analysis proposed in Fig. 4. It is observed that the scaling laws in Ra are not strongly impacted by the heterogeneity, although the prefactors for the Nu$_{\min}$ and Nu$_2$ are different, in that the compensated plots for Nu$_{\min}$ / Ra$^{-1/2}$ and Nu$_2$ / Ra$^{-1/4}$ for heterogeneous heating sources are above the data for homogeneous heating sources, pointing to the enhanced convection that we already discussed in for data in Fig. 9.
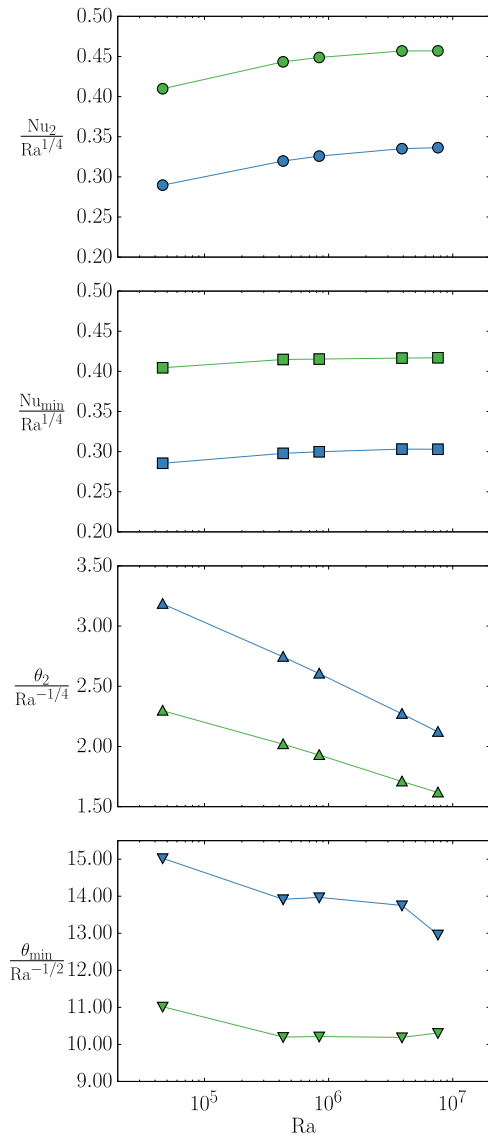
Fig. 10. Compensated plots for the scaling laws given in Eqs. (30) and (31) as a function of Ra with Ste = 1, Pr = 1. We consider simulations with a heterogeneous heating source with $\hat{\lambda}$ = 0.04: $\mathrm{Nu}_2 / \mathrm{Ra}^{1/4}$ (●), $\mathrm{Nu}_{\min} / \mathrm{Ra}^{1/4}$ (■), $\theta_2 / \mathrm{Ra}^{-1/4}$ (▲), $\theta_{\min} / \mathrm{Ra}^{-1/2}$ (▼). Also simulations with a homogeneous heating source with $T_H = T^\infty$ are considered (see text for more details): $\mathrm{Nu}_2 / \mathrm{Ra}^{1/4}$ (●), $\mathrm{Nu}_{\min} / \mathrm{Ra}^{1/4}$ (■), $\theta_2 / \mathrm{Ra}^{-1/4}$ (▲), $\theta_{\min} / \mathrm{Ra}^{-1/2}$ (▼).

5. Conclusions

This paper investigates the role of heterogeneous heating sources in the convective melting processes in PCMs using an ad-hoc model based on the Lattice Boltzmann method. The relevance of boundary conditions is known from numerical and experimental works in the literature, including the impact of variations in the temperature of the heating source [41], the role of asymmetric boundaries [42], the presence of heating sources protruding into the PCM cell [43], or the effect of porous thermal supports on PCM performance [13,39,44]. The present study introduces a twist and explores an alternative heating protocol by considering heating sources realized via alternating insulating and conductive patches. The size of the patch has been changed between simulations in order to address role of heterogeneities in the heating source. The numerical model has been validated against analytical results from the literature, as well as other numerical results for melting dynamics with homogeneous heating sources. The process of melting

has been studied by monitoring the time-dependency of the Nusselt number and the average melting front position as a function of time. Results show that the heterogeneity in the heating source impacts in a non trivial way the melting dynamics. Specifically, heterogeneous heating sources give rise to convective rolls that would be absent in the case of a homogeneous heating source. These convective rolls perturb the early (conductive) stage of the melting dynamics. Importantly, this perturbation can be controlled by the number of the insulating patches, therefore it can be tuned in a controlled way. Furthermore, thermal plumes tend to merge in the late stage of the dynamics, giving rise to oscillations in the Nusselt number. Beyond the convection effects, in presence of heterogeneous heating sources also the heated area of the source is changed. To quantitatively characterize this effect, a comparison between heterogeneous heating sources and homogeneous heating sources whose temperature has been decreased to match the average heating temperature of the heterogeneous case has been provided.

This study opens the path to future, intriguing perspectives in the field of thermal control via PCMs. First, it was found that the presence of convective rolls triggered by the heterogeneous heating source spoils the scaling-law behaviour of the Nusselt number Nu as a function of time $\mathrm{Nu} \sim \theta^{-1/2}$ in the early stages of the dynamics. Data with heterogeneous heating sources are compatible with a power-law $\mathrm{Nu} \sim \theta^{-a}$, with $a \neq 1/2$. It could also be interesting to approach the problem from a theoretical point of view, in order to understand if an actual power-law emerges and what is the relation between a and the heterogeneity size λ. Second, this study was limited to situations where the fraction of insulating patches corresponds to 50% of the whole heating source: in the spirit of other studies involving heterogeneous boundary conditions [33], it could be of interest to study the impact of different fractions, and whether these could lead to further non-linearities in the early stages of the dynamics. Finally, it could be appealing to study the way in which the heating source heterogeneities impact the melting dynamics in three-dimensional systems. In order to proceed in this direction, a more efficient code is obviously needed, and optimization work is already in progress.

Declaration of competing interest

The authors declare that they have no known competing financial interests or personal relationships that could have appeared to influence the work reported in this paper.

Data availability

Data will be made available on request.

Acknowledgements

References

[1] A. Stracke, Earth's heterogeneous mantle: A product of convection-driven interaction between crust and mantle, Chem. Geol. 330 (2012) 274–299, http://dx.doi.org/10.1016/j.chemgeo.2012.08.007.

[2] R. Yang, C.J. Howland, H.-R. Liu, R. Verzicco, D. Lohse, Morphology evolution of a melting solid layer above its melt heated from below, J. Fluid Mech. 956 (2023) A23, http://dx.doi.org/10.1017/jfm.2023.15.

[3] F. Wang, S.-D. Huang, K.-Q. Xia, Thermal convection with mixed thermal boundary conditions: effects of insulating lids at the top, J. Fluid Mech. 817 (2017) R1, http://dx.doi.org/10.1017/jfm.2017.121.

[4] Y. Lin, Y. Jia, G. Alva, G. Fang, Review on thermal conductivity enhancement, thermal properties and applications of phase change materials in thermal energy storage, Renew. Sustain. Energy Rev. 82 (2018) 2730–2742, http://dx.doi.org/10.1016/j.rser.2017.10.002.

[5] G. Müller, Convection and inhomogeneities in crystal growth from the melt, in: Crystal Growth from the Melt, Springer, 1988, pp. 1–136, http://dx.doi.org/10.1007/978-3-642-73208-9_1.

[6] S. Chandrasekhar, Hydrodynamic and hydromagnetic stability, in: Dover Books on Physics, Dover Publications, 2013, URL https://books.google.it/books?id=Mg3CAgAAQBAJ.

[7] B. Favier, J. Purseed, L. Duchemin, Rayleigh–Bénard convection with a melting boundary, J. Fluid Mech. 858 (2019) 437–473, http://dx.doi.org/10.1017/jfm.2018.773.

[8] P. Jany, A. Bejan, Scaling theory of melting with natural convection in an enclosure, Int. J. Heat Mass Transfer 31 (6) (1988) 1221–1235, http://dx.doi.org/10.1016/0017-9310(88)90065-8.

[9] Y. Dutil, D.R. Rousse, N.B. Salah, S. Lassue, L. Zalewski, A review on phase-change materials: Mathematical modeling and simulations, Renew. Sustain. Energy Rev. 15 (1) (2011) 112–130, http://dx.doi.org/10.1016/j.rser.2010.06.011.

[10] A. Samarskii, P. Vabishchevich, O. Iliev, A. Churbanov, Numerical simulation of convection/diffusion phase change problems—a review, Int. J. Heat Mass Transfer 36 (17) (1993) 4095–4106, http://dx.doi.org/10.1016/0017-9310(93)90071-D.

[11] W. Fu, X. Yan, Y. Gurumukhi, V.S. Garimella, W.P. King, N. Miljkovic, High power and energy density dynamic phase change materials using pressure-enhanced close contact melting, Nat. Energy 7 (3) (2022) 270–280, http://dx.doi.org/10.1038/s41560-022-00986-y.

[12] L.F. Cabeza, A. Castell, C.d. Barreneche, A. De Gracia, A. Fernández, Materials used as PCM in thermal energy storage in buildings: A review, Renew. Sustain. Energy Rev. 15 (3) (2011) 1675–1695, http://dx.doi.org/10.1016/j.rser.2010.11.018.

[13] L.F. Cabeza, Advances in thermal energy storage systems: Methods and applications, in: Advances in Thermal Energy Storage Systems, Elsevier, 2021, pp. 37–54, http://dx.doi.org/10.1016/B978-0-12-819885-8.00002-4.

[14] M.C. Argyrou, P. Christodoulides, S.A. Kalogirou, Energy storage for electricity generation and related processes: Technologies appraisal and grid scale applications, Renew. Sustain. Energy Rev. 94 (2018) 804–821, http://dx.doi.org/10.1016/j.rser.2018.06.044.

[15] M. Esen, T. Ayhan, Development of a model compatible with solar assisted cylindrical energy storage tank and variation of stored energy with time for different phase change materials, Energy Convers. Manage. 37 (12) (1996) 1775–1785, http://dx.doi.org/10.1016/0196-8904(96)00035-0.

[16] M. Esen, A. Durmuş, A. Durmuş, Geometric design of solar-aided latent heat store depending on various parameters and phase change materials, Sol. Energy 62 (1) (1998) 19–28, http://dx.doi.org/10.1016/S0038-092X(97)00104-7.

[17] M. Esen, Thermal performance of a solar-aided latent heat store used for space heating by heat pump, Sol. Energy 69 (1) (2000) 15–25, http://dx.doi.org/10.1016/S0038-092X(00)00015-3.

[18] S. Mellouli, N.B. Khedher, F. Askri, A. Jemni, S.B. Nasrallah, Numerical analysis of metal hydride tank with phase change material, Appl. Therm. Eng. 90 (2015) 674–682, http://dx.doi.org/10.1016/j.applthermaleng.2015.07.022.

[19] A.L. Facci, M. Lauricella, S. Succi, V. Villani, G. Falcucci, Optimized modeling and design of a PCM-enhanced H2 storage, Energies 14 (6) (2021) 1554, http://dx.doi.org/10.3390/en14061554.

[20] G. Amati, S. Succi, G. Falcucci, Enhancing the power performance of latent heat thermal energy storage systems: The adoption of passive, fractal supports, Energies 16 (19) (2023) 6764, http://dx.doi.org/10.3390/en16196764.

[21] X. Dong, H. Zhao, H. Li, G. Fucucci, Q. Zheng, H. Zhao, J. Pu, A novel design of a metal hydride reactor integrated with phase change material for H2 storage, Appl. Energy 367 (2024) 123321, http://dx.doi.org/10.1016/j.apenergy.2024.123321.

[22] B. Zalba, J.M. Marín, L.F. Cabeza, H. Mehling, Review on thermal energy storage with phase change: materials, heat transfer analysis and applications, Appl. Therm. Eng. 23 (3) (2003) 251–283, http://dx.doi.org/10.1016/S1359-4311(02)00192-8.

[23] Y. Tao, Y. You, Y. He, Lattice Boltzmann simulation on phase change heat transfer in metal foams/paraffin composite phase change material, Appl. Therm. Eng. 93 (2016) 476–485, http://dx.doi.org/10.1016/j.applthermaleng.2015.10.016.

[24] H. Nazir, M. Batool, F.J.B. Osorio, M. Isaza-Ruiz, X. Xu, K. Vignaroorban, P. Phelan, A.M. Kannan, et al., Recent developments in phase change materials for energy storage applications: A review, Int. J. Heat Mass Transfer 129 (2019) 491–523, http://dx.doi.org/10.1016/j.ijheatmasstransfer.2018.09.126.

[25] A.G. Bathelt, R. Viskanta, Heat transfer and interface motion during melting and solidification around a finned heat source/sink, J. Heat Transfer 103 (4) (1981) 720–726, http://dx.doi.org/10.1115/1.3244532.

[26] Q. Li, K.H. Luo, Q. Kang, Y. He, Q. Chen, Q. Liu, Lattice Boltzmann methods for multiphase flow and phase-change heat transfer, Prog. Energy Combust. Sci. 52 (2016) 62–105, http://dx.doi.org/10.1016/j.pecs.2015.10.001.

[27] J. Bellan, L. Selle, Large eddy simulation composition equations for single-phase and two-phase fully multicomponent flows, Proc. Combust. Inst. 32 (2) (2009) 2239–2246, http://dx.doi.org/10.1016/j.proci.2008.06.005.

[28] R. Woolley, M. Fairweather, C. Wareing, S. Falle, C. Proust, J. Hebrard, D. Jamois, Experimental measurement and Reynolds-averaged Navier–Stokes modelling of the near-field structure of multi-phase CO2 jet releases, Int. J. Greenh. Gas Control. 18 (2013) 139–149, http://dx.doi.org/10.1016/j.ijggc.2013.06.014.

[29] M. Goodarzi, M.A. Elkotb, A.K. Alanazi, H.M. Abo-Dief, I.B. Mansir, V. Tirth, F. Gamaoun, Applying Bayesian Markov chain Monte Carlo (MCMC) modeling to predict the melting behavior of phase change materials, J. Energy Storage 45 (2022) 103570, http://dx.doi.org/10.1016/j.est.2021.103570.

[30] R. Mabrouk, H. Dhahri, H. Naji, S. Hammouda, Z. Younsi, Lattice Boltzmann simulation of forced convection melting of a composite phase change material with heat dissipation through an open-ended channel, Int. J. Heat Mass Transfer 153 (2020) 119606, http://dx.doi.org/10.1016/j.ijheatmasstransfer.2020.119606.

[31] G. Seiden, S. Weiss, J.H. McCoy, W. Pesch, E. Bodenschatz, Pattern forming system in the presence of different symmetry-breaking mechanisms, Phys. Rev. Lett. 101 (21) (2008) 214503, http://dx.doi.org/10.1103/PhysRevLett.101.214503.

[32] S. Weiß, G. Seiden, E. Bodenschatz, Pattern formation in spatially forced thermal convection, New J. Phys. 14 (5) (2012) 053010, http://dx.doi.org/10.1088/1367-2630/14/5/053010.

[33] P. Ripesi, L. Biferale, M. Sbragaglia, Natural convection with mixed insulating and conducting boundary conditions: low-and high-Rayleigh-number regimes, J. Fluid Mech. 742 (2014) 636–663, http://dx.doi.org/10.1017/jfm.2013.671.

[34] S. Toppaladoddi, S. Succi, J.S. Wettlaufer, Roughness as a route to the ultimate regime of thermal convection, Phys. Rev. Lett. 118 (2017) 074503, http://dx.doi.org/10.1103/PhysRevLett.118.074503.

[35] J. Salort, O. Liot, E. Rusaouen, F. Seychelles, J.-C. Tisserand, M. Creyssels, B. Castaing, F. Chillà, Thermal boundary layer near roughnesses in turbulent Rayleigh-Bénard convection: Flow structure and multistability, Phys. Fluids 26 (1) (2014) 015112, http://dx.doi.org/10.1063/1.4862487.

[36] W. Shyy, Computational fluid dynamics with moving boundaries, Series in Computational Methods and Physical Processes in Mechanics and Thermal Sciences, Taylor & Francis, 1995, URL https://books.google.it/books?id=IQXQIotBit8C.

[37] J. Purseed, B. Favier, L. Duchemin, E.W. Hester, Bistability in Rayleigh-Bénard convection with a melting boundary, Phys. Rev. Fluids 5 (2) (2020) 023501, http://dx.doi.org/10.1103/PhysRevFluids.5.023501.

[38] H.M. Sadeghi, M. Babayan, A. Chamkha, Investigation of using multi-layer PCMs in the tubular heat exchanger with periodic heat transfer boundary condition, Int. J. Heat Mass Transfer 147 (2020) 118970, http://dx.doi.org/10.1016/j.ijheatmasstransfer.2019.118970.

[39] M. Maggini, G. Falcucci, A. Rosati, S. Ubertini, A.L. Facci, Non-dimensional numerical analysis of coupled metal hydride-phase change material hydrogen storage system, J. Energy Storage 93 (2024) 112230, http://dx.doi.org/10.1016/j.est.2024.112230.

[40] D. Almonti, E. Mingione, V. Tagliaferri, N. Ucciardello, Design and analysis of compound structures integrated with bio-based phase change materials and lattices obtained through additive manufacturing, Int. J. Adv. Manuf. Technol. 119 (1) (2022) 149–161, http://dx.doi.org/10.1007/s00170-021-08110-2.

[41] T. Bouzennada, A. Abderrahmane, O. Younis, M. Oreijah, K. Guedri, C. Maatki, L. Kolsi, Numerical simulation of heat transfer and melting process in a NEPCM: Using new fin shape, Int. Commun. Heat Mass Transfer 143 (2023) 106711, http://dx.doi.org/10.1016/j.icheatmasstransfer.2023.106711.

[42] H. Qin, Z. Wang, W. Heng, Z. Liu, P. Li, Numerical study of melting and heat transfer of PCM in a rectangular cavity with bilateral flow boundary conditions, Case Stud. Therm. Eng. 27 (2021) 101183, http://dx.doi.org/10.1016/j.csite.2021.101183.

[43] M. Faraji, H. El Qarnia, Numerical study of melting in an enclosure with discrete protruding heat sources, Appl. Math. Model. 34 (5) (2010) 1258–1275, http://dx.doi.org/10.1016/j.apm.2009.08.012.

[44] D. Gao, Z. Chen, D. Zhang, L. Chen, Lattice Boltzmann modeling of melting of phase change materials in porous media with conducting fins, Appl. Therm. Eng. 118 (2017) 315–327, http://dx.doi.org/10.1016/j.applthermaleng.2017.03.002.

[45] R. Benzi, S. Succi, M. Vergassola, The lattice Boltzmann equation: Theory and applications, Phys. Rep. 222 (1992) 145–197, http://dx.doi.org/10.1016/0370-1573(92)90090-M.

[46] C. Huber, A. Parmigiani, B. Chopard, M. Manga, O. Bachmann, Lattice Boltzmann model for melting with natural convection, Int. J. Heat Fluid Flow 29 (5) (2008) 1469–1480, http://dx.doi.org/10.1016/j.ijheatfluidflow.2008.05.002.

[47] W.-S. Jiaung, J.-R. Ho, C.-P. Kuo, Lattice Boltzmann method for the heat conduction problem with phase change, Numerical Heat Transfer: Part B: Fundamentals 39 (2) (2001) 167–187, http://dx.doi.org/10.1080/10407790150503495.

[48] T. Inamuro, M. Yoshino, H. Inoue, R. Mizuno, F. Ogino, A lattice Boltzmann method for a binary miscible fluid mixture and its application to a heat-transfer problem, J. Comput. Phys. 179 (1) (2002) 201–215, http://dx.doi.org/10.1006/jcph.2002.7051.

[49] F. Souayfane, P.H. Biwole, F. Fardoun, Melting of a phase change material in presence of natural convection and radiation: A simplified model, Appl. Therm. Eng. 130 (2018) 660–671, http://dx.doi.org/10.1016/j.applthermaleng.2017.11.026.

[50] A. Montessori, G. Falcucci, Lattice Boltzmann modeling of complex flows for engineering applications, Morgan & Claypool Publishers, 2018, URL https://books.google.it/books?id=-j9iDwAAQBAJ.

[51] G. Falcucci, G. Amati, P. Fanelli, V.K. Krastev, G. Polverino, M. Porfiri, S. Succi, Extreme flow simulations reveal skeletal adaptations of deep-sea sponges, Nature 595 (7868) (2021) 537–541, http://dx.doi.org/10.1038/s41586-021-03658-1.

[52] R. Benzi, L. Biferale, M. Sbragaglia, S. Succi, F. Toschi, Mesoscopic modeling of a two-phase flow in the presence of boundaries: the contact angle, Phys. Rev. E 74 (2) (2006) 021509, http://dx.doi.org/10.1103/PhysRevE.74.021509.

[53] M. Sbragaglia, R. Benzi, L. Biferale, S. Succi, K. Sugiyama, F. Toschi, Generalized lattice Boltzmann method with multirange pseudopotential, Phys. Rev. E 75 (2) (2007) 026702, http://dx.doi.org/10.1103/PhysRevE.75.026702.

[54] T. Krüger, H. Kusumaatmaja, A. Kuzmin, O. Shardt, G. Silva, E.M. Viggen, The Lattice Boltzmann Method - Principles and Practice, Springer, 2016, http://dx.doi.org/10.1007/978-3-319-44649-3.

[55] S. Succi, The lattice Boltzmann equation: for fluid dynamics and beyond, Oxford University Press, 2001, URL https://books.google.it/books?id=OC0Sj_xgnhAC.

[56] K. Huang, Statistical Mechanics, vol. 18, wiley, 1987, URL https://ui.adsabs.harvard.edu/abs/1987stme.book.....H.

[57] Z. Guo, C. Zheng, B. Shi, Discrete lattice effects on the forcing term in the lattice Boltzmann method, Phys. Rev. E 65 (2002) 046308, http://dx.doi.org/10.1103/PhysRevE.65.046308, URL https://link.aps.org/doi/10.1103/PhysRevE.65.046308.

[58] H. Yoshida, M. Nagaoka, Multiple-relaxation-time lattice Boltzmann model for the convection and anisotropic diffusion equation, J. Comput. Phys. 229 (20) (2010) 7774–7795, http://dx.doi.org/10.1016/j.jcp.2010.06.037.

[59] L. Li, R. Mei, J.F. Klausner, Boundary conditions for thermal lattice Boltzmann equation method, J. Comput. Phys. 237 (2013) 366–395, http://dx.doi.org/10.1016/j.jcp.2012.11.027.

[60] G. Ahlers, S. Grossmann, D. Lohse, Heat transfer and large scale dynamics in turbulent Rayleigh-Bénard convection, Rev. Modern Phys. 81 (2) (2009) 503, http://dx.doi.org/10.1103/RevModPhys.81.503.

[61] E. Bodenschatz, W. Pesch, G. Ahlers, Recent developments in Rayleigh-Bénard convection, Annu. Rev. Fluid Mech. 32 (1) (2000) 709–778, http://dx.doi.org/10.1146/annurev.fluid.32.1.709.

[62] A. Faghri, Y. Zhang, Transport phenomena in multiphase systems, Elsevier, 2006, URL https://books.google.it/books?id=bxndY2KSuQsC.

[63] M. Faden, A. König-Haagen, E. Franquet, D. Brüggemann, Influence of density change during melting inside a cavity: Theoretical scaling laws and numerical analysis, Int. J. Heat Mass Transfer 173 (2021) 121260, http://dx.doi.org/10.1016/j.ijheatmasstransfer.2021.121260.

[64] C. Zhao, M. Opolot, M. Liu, J. Wang, F. Bruno, S. Mancin, K. Hooman, Review of analytical studies of melting rate enhancement with fin and/or foam inserts, Appl. Therm. Eng. 207 (2022) 118154, http://dx.doi.org/10.1016/j.applthermaleng.2022.118154.

[65] T. Shockner, G. Ziskind, Experimental and numerical evaluation of phase-change material performance in a vertical cylindrical capsule for thermal energy storage, Appl. Therm. Eng. 219 (2023) 119519, http://dx.doi.org/10.1016/j.applthermaleng.2022.119519.